Deformation Mechanisms and Evolution of Mechanical Properties in Damaged Advanced Ceramics

Calvin Lo[a,*], Tomoko Sano[b], James D. Hogan[a]

[a] *Department of Mechanical Engineering, University of Alberta, Edmonton, AB T6G 2R3, Canada*
[b] *Weapons and Materials Research Directorate, Army Research Laboratory, Aberdeen Proving Ground,MD 21005, USA*

Abstract

We investigated the uniaxial compressive behavior of damaged and intact alumina using quantitative X-ray computed tomography (XCT) analysis coupled with digital image correlation (DIC) for mechanical characterization. Internal three-dimensional crack characteristics such as crack surface area and orientation were quantified using XCT to assess the level of damage. From the quasi-static and dynamic stress-strain results, the primary effects of crack damage is to reduce the initial stiffness and rate of lateral expansion in damaged alumina. With increasing axial strain, crack closure was found to lead to a recovery of elastic properties, in some cases to intact levels, in the damaged specimens. Localized deformation mechanisms related to the crack structure, including lateral crack closure, axial crack opening and closing, and inclined crack sliding, were visualized in-situ and connected to XCT reconstructions. High-speed imaging also revealed a mixed fracture mode for damaged alumina that included axial splitting and failure along pre-existing cracks.

Keywords: X-ray computed tomography, fracture, digital image correlation, damage, ceramic

*Corresponding author
Email address: clo2@ualberta.ca (Calvin Lo)

1. Introduction

Advanced ceramics are commonly used to protect against ballistic threats due to their high hardness and compressive strength. In these applications, ceramic armor may be expected to defeat multiple ballistic projectiles[1], commonly referred to as "multi-hit" capability. During an impact event with a high speed projectile, the ceramic material immediately in front of the projectile often becomes comminuted, and extensive cracks develop and propagate across the surrounding region[2]. In-situ visualization of edge-on impact experiments have shown that the rate of damage propagation in brittle materials, such as glass or ceramics, far exceeds the penetration velocity of projectiles[3]. Other studies focusing on the propagation characteristics of failure fronts in brittle materials include work by Bourne et al.[4, 5] and Partom[6]. Flash x-ray photography of long rod penetration experiments with glass have also shown that penetration is outpaced by the failure front, and the projectile penetrates into damaged material[7]. Johnson and Holmquist[8] have emphasized the important role of parameters relating to damaged and failed materials for accurate impact modeling. As a result, an understanding of the behavior of damaged advanced ceramics, as well as the transition from intact to damaged material behavior, is critical to the development of improved impact models and protection products with increased multi-hit resistance. This is explored in this paper.

The lack of model parameters for damage models has motivated numerous studies focused on the behavior of damaged brittle materials[9, 10, 11]. A common approach in the literature has been to pre-damage the ceramic, followed by compression testing on the pre-damaged specimens[12, 13]. Following this approach, quasi-static confined compression experiments have been performed on a range of damaged brittle materials, including SiC-N[14], boron carbide[13], borosilicate glass[12, 15, 16, 17], and soda lime glass[18]. Typically, damage in these studies was introduced through thermal shock cycles[13], mechanical load-unload cycles[15], or a combination of both[15]. In their study, Zurek and Hunter[19] performed high strain rate confined compression experiments

on pre-damaged TiB_2 specimens using a split-Hopkinson pressure bar (SHPB). The TiB_2 specimens were pre-damaged through a flyer plate impact experiment in order to simulate the damage achieved through shock compression. In an alternative approach, Chen and Luo[20] employed two consecutive compressive waves in a modified SHPB setup to characterize the dynamic behavior of damaged alumina[21] and silicon carbide[22] under confinement. In this technique, the first wave is used to pre-damage the ceramic in-situ under dynamic compression, and the second wave is used to probe the strength of the damaged ceramic. Effort was made to vary the level of damage in all of the above studies (e.g. modifying the number of thermal shock cycles, mechanical loading cycles, shock pressure, or compressive pulse amplitude) to access different damage levels, and microscopy was often used to confirm the presence of cracks where possible. However, limited information exists on quantitative measurements of internal damage[23] and on the uniaxial compressive behavior of damaged ceramics, a configuration which is more favorable for in-situ visualization as compared to triaxial confined compression where the specimen surface is covered.

In this paper, we combine microstructural characterization and in-situ visualization to explore the compressive behavior of pre-damaged advanced ceramics. We apply X-ray computed tomography (XCT) to characterize the internal crack networks of pre-damaged alumina in order to quantify the damage level prior to testing, including crack surface area and orientation. Following damage characterization, quasi-static and dynamic compression experiments were performed to probe the mechanical response of pre-damaged specimens. The dynamic experiments were visualized in-situ using an ultra-high-speed camera to observe the failure process, and digital image correlation was employed to perform spatial strain measurements that allowed for the observation of localized deformation features in the experiments. Finally, the crack characteristics are coupled with the experimental results to connect local deformation mechanisms to the evolution of mechanical properties in damaged ceramics. This work builds on prior work by the authors where a similar approach has been applied to pre-damaged boron carbide[24] and intact alumina[25].

2. Experimental Method

2.1. Material and Specimen Preparation

The characterization and experiments in this study were carried out on AD995 alumina from Coorstek Inc. (Vista, California, US), with a manufacturer specified density of $3.90\,\mathrm{g/cm^3}$, Young's Modulus of 370 GPa, and a Poisson's ratio of 0.22. Alumina (Al_2O_3) was chosen as a model advanced ceramic as it is commonly utilized in body armor applications, and has been well studied in the literature [26, 27, 28]. The "995" refers to a nominal composition of 99.5% Al_2O_3, with the other 0.5% being comprised of silicon dioxide[29].

Cuboidal specimens with dimensions 2.3 mm by 2.7 mm by 3.5 mm were machined from as-received AD995 titles. The dimensions of the specimens were selected to accommodate both the size of the SHPB used for dynamic compression and the scan volume of the synchrotron X-ray source used for computed tomography scans. We chose to use a cuboidal shape so that digital image correlation analysis could be performed on a flat surface during the compression experiment, as discussed later in the Mechanical Testing section.

To introduce pre-damage to the specimens prior to the compression experiments, each specimen was subjected to thermal shock cycles. Using a butane blow torch, each specimen was heated to above 750 °C and then quenched in room temperature water. The number of thermal cycles, ranging from 1 to 8, was varied from specimen to specimen in order to introduce a range of damage levels amongst the different specimens. Cracks caused by the thermal cycles can be observed in the XCT scan of a pre-damaged specimen in Figure 1A, as discussed in more detail in later sections. While the thermal cycles were sufficient to cause internal cracking, all pre-damaged specimens remained structurally intact after thermal cycling.

2.2. X-ray Computed Tomography

2.2.1. X-ray Computed Tomography Scans

X-ray computed tomography was used to characterize the internal cracks in the pre-damaged specimens. Currently, XCT is capable of visualizing features

at sub-micron scales[30], however, there is a trade off between resolution and scan volume; with increasing resolution, scan volume decreases. For this study, it is important to have the resolution high enough to resolve internal cracks, which have crack widths on the order of several microns, but also a scan volume large enough to encompass the test specimen and avoid sampling issues. A partial scan may not accurately capture a representative level of damage since the cracks are not necessarily uniformly distributed throughout the volume of the samples. Based on these considerations, the specimens were scanned with a resolution of 1.75 µm and a scan volume spanning 2.196 mm by 3.413 mm by 3.413 mm, which is approximately 93% of the total specimen volume. All XCT scans were performed using the Skyscan micro-CT system on the 05ID-2 POE-2 endstation[31] at the Biomedical Imaging and Therapy (BMIT) beamline at the Canadian Light Source synchrotron facility (Saskatoon, Saskatchewan, Canada). Ring artifacts were removed using a low-pass Gaussian filter[32]. Figure 1A shows a reconstructed XCT scan for a pre-damaged AD995 specimen. Macroscopic cracks can clearly be seen in the magnified view, and SEM has confirmed that the small dark features in the XCT scans are internal pores[25].

2.2.2. Image Segmentation and Post-processing

To reconstruct the crack networks digitally, the first step is to apply image segmentation to isolate the cracks in the XCT scans. During image segmentation, the pixels that represent the features of interest, in this case, cracks, are segregated to form binary images where foreground pixels (1's) represent crack area and background pixels (0's) represent other constituents. Note that the small unconnected pores are not to be included in the reconstruction because they are present in the intact material. Cracks are the only form of structural damage considered in this study. An entropy filter[33] is applied to the grayscale image to enhance the crack edges in the scans, and then locally adaptive thresholding[34], computed using the mean intensity of the grayscale values in the neighborhood of each pixel, is applied to segment the grayscale image.

Following segmentation, a number of 2D filtering and processing operations

are required to remove noise and other microstructural constituents from the binary image. Non-physical features may be introduced to the binary image due to over-segmentation or scan artifacts, and these are typically in the form of salt and pepper noise[35]. Owing to the grayscale difference between the pores and the surrounding alumina grains, the pores also become segmented into the foreground. In addition, due to local variations in the scan contrast, the crack area may not be fully segmented, leading to gaps in the binarized crack network. To distinguish crack area from pores and point-like over-segmentation noise, all of the objects in a binary image are filtered based on a combination of object area, aspect ratio, and extent. *Extent* is the ratio between the object area and the area of the bounding box. For the pores and point-like noise, the area is small, and both the extent and the aspect ratio are expected to be close to unity. In contrast, long connected cracks are expected to have a larger area, a lower aspect ratio, and a lower extent. These filters are applied in combination using logical 'AND' to prevent the exclusion of unconnected crack areas which may be small but have a low aspect ratio.

After post-processing, the binary images are combined into a 3D binary matrix, and connected components analysis is performed (using 26 connectivity) to identify the 3D objects formed by the 2D binary slices. From the XCT scan in Figure 1A, it can be seen that the cracks are on the scale of the specimen and are much larger in volume than individual pores. Therefore, the reconstructed 3D volumes were filtered based on volume to further remove any pores or noise that were not removed during 2D filtering. As mentioned previously, the crack area in each XCT scan may not be fully segmented, and this can lead to gaps in the 3D reconstructed crack network. To fill out the gaps and complete the crack network, morphological closing was applied to the 3D binary matrix. Morphological closing[36] involves the dilation of a binary matrix by a structuring element followed by the erosion of the dilated matrix by the same structuring element. It is attractive in this application because it systematically dilates the binary object, closing any gaps, and then erodes the dilated object to return the object to its original size with the gaps closed. A spherical structuring element

was used to preserve the shape of the crack network. A rendering of the final reconstructed crack network for one specimen can be seen in Figure 1B. The red box indicates the boundary of the XCT scan volume. It can be seen that the cracks are largely planar, span much of the sample, and are well connected. For each specimen, connected components analysis revealed that the reconstructed objects are few in number but large in volume, which confirms that the cracks are mostly connected. The crack networks in these thermally shocked specimens are therefore dominated by a few large crack planes as opposed to many isolated micro-cracks.

2.2.3. Crack Characterization

Due to the complexity, interconnectedness, and randomness of the crack networks in the pre-damaged specimens, the effects of crack damage may be assumed to be isotropic, in which case a scalar damage metric would be appropriate. Scalar metrics for characterizing cracks include crack density, volume, and surface area. Landis[23] and Oesch et al.[37] have investigated crack surface area and volume as scalar damage metrics in in-situ XCT investigations of concrete. Crack density, typically used to consider micro-cracks[38], is not applicable in this study since the cracks are large and interconnected. With increasing thermal cycles, the cracks become more interconnected and the number of cracks actually decrease. Based on analysis of individual scans, crack widths range from 3 µm at the thinner range to 70 µm for the larger cracks. Given the resolution of the scans, it is difficult to distinguish between a closed crack and a crack width less than 3 µm. Due to the X-ray attenuation at the free surface, thin or closed cracks that form parts of larger crack networks can still be distinguished by their grayscale contrast. Therefore, crack volume measurements may be overestimated by the inclusion of closed or thin cracks. While closed cracks may not contribute to the total crack volume, they are expected to have an effect on the mechanical response. As a result, surface area may serve as a better crack characteristic in this type of specimen configuration in comparison to crack volume because it can be more accurately quantified for thin cracks.

Alternatively, anisotropic local deformation related to the internal cracks, such as frictional sliding or crack closure, will depend on crack orientation[39, 40]. Traditional definitions for crack orientations are based on the crack normal, which is easy to compute for idealized planar cracks. However, three-dimensional cracks may branch off, reconnect, and curve, as shown in Figure 1B. This complicates the process of determining a crack normal, as the reconstructed cracks in these types of specimens are well connected and seldom planar. The crack network must be discretized for the quantification of crack normals. To do this, we apply the Marching Cubes algorithm[41], a technique for generating an isosurface from a three-dimensional binary matrix that is commonly used to visualize XCT data[42]. Marching Cubes produces a mesh comprised of triangles, from which the crack orientation can be computed. Using the vertices of the triangles, we can calculate both the surface normal vector and surface area of the triangle. Once the surface vectors are known, the orientation of the crack surface with respect to any direction can be computed. The orientation of interest in this study is the angle between the loading axis of the specimen (along the 3.5 mm dimension) and the surface normal vector. Since the area of individual triangles are also known, the area contribution of surfaces with a given orientation can be quantified. The total crack surface area can then be computed by summing over all triangles. Note that the triangles do not all have the same area. To give an idea of the level of discretization, Marching Cubes generates over 2,000,000 triangles for the mesh of one specimen's crack network.

2.3. Mechanical Testing

A Material Testing System (MTS) 810 load frame was used to carry out quasi-static uniaxial compression experiments. Using displacement control, the specimens were compressed along the long dimension (3.5 mm) at a rate of 3.5×10^{-3} mm/s to achieve to a nominal strain rate of $1 \times 10^{-3}\,\mathrm{s}^{-1}$. Due to the compliance of the loading frame, the actual strain rate, as measured using digital image correlation, is approximately an order of magnitude lower. Tungsten carbide platens confined in titanium were used at the interface between the com-

pression platens and the ceramic samples to prevent the alumina from indenting into the platens. High-pressure grease was used to lubricate the platen-ceramic interface and facilitate free lateral expansion. The specimen surface was visualized at 100 frames per second (FPS) at a resolution of 850 by 850 pixels using a Promon U750 high speed camera. This frame rate is insufficient for capturing the fracture process in the quasi-static experiments. Intact specimens were also tested to serve as a reference to the damaged specimens.

A split-Hopkinson pressure bar (SHPB) was used to perform dynamic uniaxial compression experiments. All bars in the apparatus have a diameter of 12.7 mm and are made of maraging steel with a stiffness of 200 GPa and a density of 8100 kg/m^3. The incident and transmission bars measure 1000 mm and 910 mm, respectively. As in the quasi-static tests, titanium jacketed tungsten carbide platens and high pressure grease were used at the platen-ceramic interface. The impedance of the tungsten carbide platens are matched to the incident and transmitted bars to reduce wave reflection at the interfaces. A 304 mm long striker and a tin pulse shaper with a diameter of 3.175 mm and a thickness of 1 mm were used to create the incident wave. This combination generates a triangular pulse with a rise time of 230 µs. During the compression experiments, a Shimadzu HPV-X2 ultra-high-speed camera was used to visualize the surface of the specimen at 500,000 FPS with an exposure time of 1000 ns. A total of 128 frames measuring 400 by 250 pixels was recorded for each experiment. Beyond recording the dynamic compression event, this frame rate also captures the fracture and fragmentation process.

Digital image correlation (DIC) was used to make surface strain measurements at both quasi-static and dynamic rates. Two-dimensional DIC is a computer vision method for computing surface strains[43, 44]. In this technique, the contrast on the specimen surface is commonly enhanced through the application of a speckle pattern. Experimental challenges relating to the application of DIC in this study include the generation of a fine speckle pattern required for small specimens and adequate lighting for filming at high frame rates. To address these challenges, an airbrush with a 0.15 mm diameter nozzle was used

to produce a fine speckle pattern (i.e. 5 to 10 pixels per speckle) appropriate for DIC measurements. An LED ring light array from REL Inc. was used to illuminate the specimen surface during dynamic experiments, and a silver reflective paint was used to generate the speckle pattern to enhance surface reflectivity. DIC analysis was performed using VIC-2D (v6 2018) from Correlated Solutions (Irmo, South Carolina, US). We used a subset size of 27 pixels, a step size of 7 pixels, the zero-normalized sum of squared differences criterion, and the optimized 8-tap interpolation scheme[45] to perform correlation analysis. The engineering strain tensor was used to calculate the strains.

Stress-strain curves were produced by matching the computed strain profiles to the stress histories. The peak strain and peak stress were matched in time through MATLAB to correlate the rest of the strain and stress profiles. The stress profiles from the quasi-static experiments were measured using the MTS load cell. The stress profiles from the dynamic experiments were calculated using strains from the transmitted strain gauge as follows:

$$\sigma\left(t\right) = E\frac{A_0}{A_B}\epsilon_T(t) \tag{1}$$

The stress in the specimen σ (Pa) is computed based on the Young's Modulus of the transmitted bar E (Pa), the area of the specimen cross-section A_0 (m^2), the transmitted bar area A_B (m^2), and the strain from the transmitted gauge $\epsilon_T(t)$, as a function of time t (s). Using a linear fit of the strain-time profiles, strain rates in the quasi-static experiments were found to be range from 1.6 to $2.3 \times 10^{-4}\,s^{-1}$ and strain rates in the dynamic experiments were found to range from 6.8 to $13.1 \times 10^{1}\,s^{-1}$. The application of 2D DIC for characterizing stress-strain behavior is typically based on the assumption that the surface measurement is representative of the overall strain profile for the specimen[46]. Given the inhomogeneous nature of cracked specimens, it is not strictly accurate to match the stress profile to the strain profile for damaged specimens, as the stress profile is a measure of the overall response to force while the strain profile is a measure of the deformation on only one surface. The deformation of each

specimen surface is expected to differ depending on the pre-existing cracks on that surface, so surface measurements may not be representative of the overall response, unlike in intact specimens. Currently, there are limited methods for characterizing the development of inhomogeneous three-dimensional strains under compressive loading. One method is to combine XCT visualization with in-situ compression testing[47]. However, such setups are not easily accessible, and strains cannot be continuously measured due to the time required to perform XCT scans, during which the specimen may also relax. In addition, XCT scan times preclude visualization of ceramics under dynamic compression. For these reasons, we have chosen to compute the stress-strain behavior of damaged ceramics in this study by matching surface strain measurements to the stress profiles and emphasize that it is an approximation.

3. Results

3.1. Crack Orientation and Surface Area

First we begin by presenting the crack characterization results. The stacked bar chart in Figure 2 shows the crack surface area quantified using XCT for each specimen. Specimens are named with the following conventions: quasi-static tests are denoted by "QS", dynamic tests are denoted by "DYN", damaged specimens are denoted by "D" in front of the test number, and intact specimens are denoted by "IN" in front of the test number. The total crack surface area for each specimen is divided into segments showing the area contribution of crack surfaces that form different angles with respect to the loading axis in 10 degree intervals. This is done to illustrate the distribution of crack orientations within each specimen. Overall, the crack area in each orientation interval generally increases as total crack area is increased. As well, there are no major differences between the relative contributions of different crack orientations across most of the specimens. One exception is specimen DYN D1, which has a relatively low amount of crack surface area between 0° and 10° and a relatively large amount of crack surface area between 30° and 40° given its low total crack surface area.

The 3D reconstruction for DYN D1 shows that the crack pattern in this specimen is dominated by a large inclined crack, which is responsible for the preference for the angles between 30° and 40°. Cracks with different orientations with respect to the loading axis are expected to have different effects on the deformation of the specimen, as will be shown in Section 3.3. With these crack measurements, we can connect the damage in individual specimens to differences in mechanical behavior, such as crack closure transition strains (Section 4.1) or compressive strength (Section 4.2).

3.2. Quasi-static and Dynamic Compression Experiments

Next, we present the quasi-static and dynamic compression results. The stress-strain and lateral-axial strain curves for the quasi-static and dynamic compression experiments are shown in Figure 3A and Figure 3B, respectively. The intact specimens exhibit mostly linear elastic behavior at both strain rates, as shown by the linear stress-strain and lateral-axial strain curves. Closer to the failure strain, the intact stress-strain curves deviate from linearity due to surface chipping, which destabilizes the strain field. From the quasi-static experiments, the intact AD995 specimens have an average failure strain of 0.71 ±0.05%, peak compressive stress of 2.6 ±0.2 GPa, stiffness of 380 ±20 GPa, and Poisson's ratio of 0.23 ±0.02. From the dynamic experiments, the intact AD995 specimens have an average failure strain of 1.1% ±0.1%, peak compressive stress of 3.9 ±0.1 GPa, stiffness of 370 ±10 GPa, and Poisson's ratio of 0.24 ±0.03. The rate dependent increase in strength and failure strain is well-documented for advanced ceramics[48].

Based on the stress-strain data in Figure 3A and Figure 3B, it can be seen that crack closure dominates the deformation of damaged specimens at both strain rates during the early stage of compression. Since the pre-existing cracks in the damaged specimens are more compliant than the solid material, the cracks will close over axially before the intact material is compressed. This crack closure behavior is reflected in the stress-strain curves in Figure 3A and Figure 3B by the low initial stiffness and the subsequent increase in stiffness as

the specimens undergo further compression. As the cracks close, the stiffer intact material becomes compressed, thereby increasing the overall stiffness of the specimen. For specimens QS D2, QS D4, DYN D1, and DYN D5 in Figure 3A and Figure 3B, the increase in stiffness is accompanied by a linearization of the stress-strain curve after closure, and the recovered stiffnesses, ranging from 357 to 387 GPa, are maintained until close to failure. This shows that the intact stiffness may be fully recovered in damaged specimens following crack closure at these damage levels. The lateral strain curves in the lower halves of Figure 3A and Figure 3B are also consistent with the crack closure interpretation. Since crack volume is expected to dominate much of the initial axial strain, there should be minimal lateral expansion, and this is the case for most of the damaged specimens (e.g., QS D2 and DYN D5). For specimens QS D3, DYN D1, and DYN D3, the initial negative lateral strain suggests that crack closure can actually lead to contraction in some cases, and this is likely due to the orientation of the pre-existing cracks in the specimen (e.g., inclined and axial cracks intersecting at an acute angle). Furthermore, the axial strain at which the lateral strain begins to increase is consistent with the axial strain at which the stiffness markedly increases. After the cracks are closed, the compression of intact material will lead to an increase in overall lateral strain, which should coincide with the increase in stiffness. Though it is more difficult to see in the other specimens, this transition can be clearly observed in Figure 3A for specimen QS D4 at an axial strain of 0.48%, and in Figure 3B for specimen DYN D5 at an axial strain of 0.40%. For other specimens, such as QS D1 and DYN D2, the intact stiffness is never fully recovered. Instead, the gain in stiffness from crack closure is believed to be offset by the loss of stiffness from the growth of pre-existing cracks or nucleation of new cracks. The large increases in lateral strain shown in the inset on Figure 3A are caused by the opening of axial cracks in specimen QS D1 (as will be shown visually later in Figure 4A), and each sudden increase correlates with a change in slope for the stress-strain curve.

After crack closure, it can be seen from Figure 3A and Figure 3B that the lateral strains rise faster for the damaged specimens than for the intact

specimens, which indicates that the rate of lateral expansion in the damaged specimens has exceeded the Poisson's ratio of the intact material. This shows that lateral crack opening is contributing to lateral expansion in addition to the elastic expansion of solid material in the damaged specimens. As well, the softening of the stress-strain curve near the failure strain is accompanied by a sharp increase in lateral expansion for several specimens (e.g., QS D4, DYN D2, DYN D5), indicating catastrophic crack growth leading to macroscopic failure. While the stages may differ in length for each specimen, all the damaged specimens exhibit crack closure, followed by an increase in stiffness, and then a loss of stiffness leading to failure. To the author's knowledge, this has not been noted before in the literature.

Where results from the two strain rate regimes for the damaged materials differ are in the failure strains and in the rate of lateral expansion following crack closure. Pre-existing cracks may degrade the strength of the specimen and cause failure at a lower axial strain. At the same time, the compliance of the cracked regions reduce the overall stiffness of the specimen and allow for greater axial strains to be achieved. The influence of damage on failure strain is controlled by these competing failure mechanisms. In the quasi-static tests, the additional strain from crack closure contribute significantly to the failure strain, as all of the damaged specimens exhibit greater failure strains than the intact specimens. In contrast, the failure strains for the damaged specimens in the dynamic experiments are comparable to or lower than those of the intact specimens, which suggests that the strength degradation is more critical in dynamic loading. In general, the dynamic damaged specimens also show an increased rate of lateral expansion in comparison to the quasi-static damaged specimens, signaling increased crack opening at higher strain rates and, thus, different damage accumulation behavior. Taken together, these differences show that pre-existing damage has a greater effect on the compressive strength under dynamic strain rates than quasi-static strain rates.

3.3. Localized Deformation in Damaged Ceramics

Next we examine the DIC strain contours computed from the quasi-static experiments to explore localized deformation features in damaged advanced ceramics. Crack opening can be visualized in DIC by the development of localized positive lateral strain. Shown in Figure 4A is a lateral strain contour plot of specimen QS D1, where the opening of a large axial crack can be observed in the figure. This crack opening corresponds to the first large increase in lateral strain for QS D1 at an axial strain of 0.30% in Figure 3A and is the cause of the relatively low strength of QS D1 (1.88 GPA vs 2.60 GPa). The second sudden increase in the lateral strain for QS D1, at an axial strain of 0.34% in the inset in Figure 3A, is also connected to the opening of a second axial crack on the surface. Shown in Figure 4B is a lateral strain contour plot of specimen QS D3, which also has a large axial crack. However, rather than a region of localized positive lateral strain, this crack is outlined by a region of negative lateral strain, which suggests that the crack is actually accommodating the expansion of the adjacent solid material, and the crack does not open throughout the test. This mechanism may compete with crack growth and solid material compression, both of which lead to increased lateral expansion, to reduce the overall lateral expansion of the specimen (i.e., the axial crack becomes closed).

Figure 4C shows the surface of specimen QS D4 visualized through XCT. By overlaying the XCT scan in Figure 1A with the DIC contours, localized deformation features can be connected to the physical structure of the crack network. The contrast in this XCT scan has been enhanced through an entropy filter[33] to highlight the cracks. Specimen QS D4 is used as a representative sample because it exhibits the different types of localized strains observed for damaged specimens in this study and demonstrates deformation mechanisms associated with different crack orientations. Shown in Figure 4D is an axial strain contour plot of QS D4 with the crack pattern overlay. This direct observation of crack closure shows the localized compressive strains that develop at lateral and low-angled inclined cracks under uniaxial compression. The lateral strain contour plot of QS D4 in Figure 4E shows negative lateral strains

developing at axial and high-angled inclined cracks. Similar to specimen QS D3, the expansion of the nearby intact material effectively closes the axial and high-angled cracks. Under compressive loading, inclined crack surfaces may slide against each other following crack closure, as noted in micro-cracks based micro-mechanical models[49, 40]. This frictional sliding behavior can be observed through the shear contour plot shown in Figure 4F. White arrows have been added to Figure 4F to show the relative motion of the crack surfaces. Negative shear develops along crack surfaces inclined towards the right edge of the specimen, and positive shear develops along crack surfaces inclined towards the left. These are all examples of how cracks with different orientations can cause localized strains to develop and influence the macroscopic mechanical response of the specimen.

Beyond the spatial variation in strains, DIC was also used to track the evolution of local deformation through time to explore the effects of crack orientation on localized axial and shear strain. Figure 5A shows the XCT scan of specimen QS D4 overlaid with 7 regions where the local strains were queried. The 7 regions correspond to a range of different structural features, including solid material, axial cracks, inclined cracks, triple junctions, and lateral cracks. Figure 5B shows the temporal evolution of axial strain at each of these locations. First, we note that the triple junction (region 6), which has a relatively large crack volume, and the lateral crack (region 7), which is perpendicularly oriented to the loading direction, deform at the greatest rates. As the angle of the crack with respect to the loading direction is reduced, the rate of axial deformation is decreased, as shown by the two inclined cracks (regions 4 and 5) and the axial crack (region 3). Finally, the intact sections (regions 1 and 2) deform at the slowest rate due to the relatively high stiffness. It is interesting to note that the deformation rates are initially identical for the regions of high compliance; the axial strain profiles for regions 6 and 7 evolve similarly up until a time of 12 seconds, at which point they begin to deviate. Similarly, the separate regions of intact material (regions 1 and 2) experience nearly identical strains throughout the entire experiment.

To investigate the evolution of frictional sliding between crack faces, shear strain is plotted against axial strain at each of these regions in Figure 5C. As expected, there is minimal shear strain at the two intact regions, the lateral crack, and the axial crack. The slopes of the shear-axial strain curves for the triple junction and the inclined cracks indicate that the axial and shear strains are coupled. In other words, crack closure and crack sliding occur simultaneously under loading. Shear strain at the triple junction is arrested at an axial strain of 0.9% and does not develop further under additional axial strain, while shear strain at the inclined crack at region 4 continues to increase until failure. This may explain the divergence in axial deformation between the triple junction and the lateral crack: the shear strain at region 4 continues to accommodate additional axial strain at the triple junction while the lateral strain is constrained by crack closure. Since a frame rate of 100 FPS is insufficient for capturing the fracture process of the specimen, it is not possible to determine which local feature ultimately causes the specimen fail in the quasi-static experiments. As this is only one view of the specimen, it may also be the case that failure is caused by a feature that is not visualized on this surface. In contrast to the quasi-static experiments, where the temporal resolution is limited and the spatial resolution is high, visualization of the dynamic experiments is limited by spatial rather than temporal resolution. While localized strain in the dynamic experiments are also observed in the contour plots generated through DIC, their shapes are not very exact. Therefore, we will not be performing similar analysis with the dynamic experiments.

3.4. Failure Process of Damaged Ceramics

With the Shimadzu HPV-X2 imaging at 500,000 FPS, it was possible to capture the post-peak failure process during the dynamic compression experiments. Figure 6 shows a comparison of the stress-time histories and failure process for an intact specimen (DYN IN4) and a damaged specimen (DYN D5) under dynamic loading. Red arrows point to the first surface cracks visualized in Figure 6. For the intact specimen, the first surface cracks initiate at the

right edge of the specimen immediately after peak stress is reached at a time of 144 µs. The cracking spreads along the right edge of the specimen, and a large axial crack propagates along the top of the specimen. Note that at a time of 152 µs, the bottom left corner of the specimen still has not moved or cracked, indicating that part of the specimen is still load-bearing. Finally, at 160 µs, the specimen is fully fragmented and no longer bears any load. It can be seen that the fragments are long and oriented parallel to the loading direction, similar to the axial splitting observed for other advanced ceramics. This fracture behavior is consistent with the failure process observed in high-speed visualization of SPHB tests on other advanced ceramics (e.g., boron carbide [50, 51]).

For the damaged specimen, the initial surface damage develops in the middle of the specimen along pre-existing cracks rather than at the edges. Isolated cracks begin to grow simultaneously across the specimen surface at a time of 138 µs, then coalesce at 144 µs, leading to the failure of the specimen. At 154 µs, the specimen is fully fragmented. Unlike the axial cracks that dominate the fracture of the intact specimens, the damaged specimen shows a mix of inclined and axial cracking. The large inclined cracks are attributed to the opening of pre-existing cracks. Axial cracks can be observed in the top right and bottom left corners of the specimen at 154 µs, which only initiate after the major inclined cracks have coalesced at 144 µs. Axial splitting was also observed in the initially crack-free regions of damaged specimens in other dynamic tests. Overall, the fragments observed at 154 µs are larger for the pre-damaged specimens than for the intact specimens.

4. Discussion

This study explores local deformation features and the effects of crack damage on mechanical response of damaged AD995. To quantify the level of damage in pre-damaged specimens, XCT was applied to characterize the internal crack networks. Quasi-static and dynamic compression experiments were performed to characterize the rate-dependent mechanical response of intact and

pre-damaged specimens. In the discussion section, we connect physical crack damage parameters to the degradation of mechanical properties in damaged ceramics, and then discuss the implications of the results in this paper in the context of ballistic response and computational modeling of material behavior.

4.1. Relationship Between Crack Orientation and Crack Closure

As noted in Section 3.2, the stiffness of the damaged specimens increase with crack closure up until a transition strain, at which point the majority of the cracks are closed and the stiffness stops increasing. Similar stiffening behaviors have been observed in excavated rocks[52], and past investigators have studied the stress threshold required to close cracks in brittle rocks[53, 54]. In this study we connect crack closure strains to XCT crack measurements. Based on the contour analysis in Section 3.3, cracks oriented between 0° and 40° with respect to the loading axis contribute most significantly to localized axial strains, as they coincide with the greatest localization of compressive axial strain. Beyond this range, localized axial strains decrease with increasing angle with respect to the loading axis, up to a maximum angle of approximately 60°, above which the inclined and vertical cracks experience similar axial strains to the undamaged parts of the specimen. Therefore, crack surfaces with orientations between 0° and 60° are believed to contribute most to the crack closure strain. To estimate the transition strain that signals the effective closure of pre-existing cracks, we applied a moving window regression approach[53] to compute the stiffness of the damaged specimens and defined the transition strain as the first point at which the stiffness stabilizes at a constant value. This axial strain typically also marks the point at which the lateral strain linearizes. The estimated transition strains for the damaged specimens are plotted on Figure 7 as a function of the crack surface area for orientations between 0° and 60° for each specimen. Overall, it can be seen that the transition strain increases with increasing low-angle crack area, with the exception of few dynamic tests. For the two dynamic tests with the lowest crack surface area (DYN D1 and DYN D2), the transition strains are higher than expected when compared to the quasi-static tests with

similar crack area (QS D1 and QS D2). The dynamic test with the greatest damage, DYN D4, also shows a much lower transition strain than expected. Despite significant differences in crack surface area, DYN D4 has a transition strain similar to that of DYN D3. Deviations from the trend of increasing crack closure strain with increasing low-angle crack area may be attributed to variations in crack thicknesses and loading rates. In comparing the crack surface orientation to the transition strain, we assume that the cracks are of similar thicknesses across different orientations for different specimens. However, it is possible, for example, that some specimens have fewer low-angle cracks with greater thicknesses while other specimens have more low-angle cracks that are thinner or closed. In these cases, the specimen with the fewer, but thicker, cracks may experience a greater closure strain. Therefore, a certain level of scatter is to be expected. As well, under quasi-static compression, the crack surfaces have time to slide and shift past asperities for maximum closure, but under dynamic compression, the load is applied so quickly that the cracks may not have enough time to close completely before failure starts. Consequently, the scatter in transition strain is expected to be greater for the dynamic regime than for the quasi-static regime.

4.2. Relationship Between Crack Surface Area and Strength

The quasi-static and dynamic strength results are plotted against XCT crack surface area measurements in Figure 8. Across the range of crack damage accessed, there is no clear relationship between crack surface area and quasi-static strength. The weakest specimen tested in quasi-static compression, QS D1, has the lowest crack surface area, while the strength of the other damaged specimens are within the scatter of intact quasi-static strength measurements. From the contour plot in Figure 4A, it is clear that the opening of the axial crack causes QS D1 to fail. This suggests that the extent of overall crack damage is not as critical for quasi-static compression. Instead, fracture is likely governed by the most deleterious crack, which would lead to more stochastic results in the quasi-static regime, as is commonly assumed in the literature. As noted in Sec-

tion 3.3, even though both specimens QS D1 and QS D3 both have large axial cracks, the effects of the axial cracks on the mechanical response are dramatically different for the two specimens. Alternatively, if the transition from intact to failed material is instantaneous, as assumed by the JH-1 model[55], then it is possible that the range of damage accessed in this study did not reach the transition point. More data is required to determine the relationship between crack damage and quasi-static strength.

In contrast, the dynamic experiments show decreasing strength with increasing crack surface area over the damage levels accessed in this study. This trend is consistent with the JH-2 model[56] assumption that the transition from intact to failed material is gradual. From the dynamic experiments, it was found that the damaged specimens exhibited a greater rate of lateral expansion than the intact specimens. This suggests that the presence of pre-existing cracks leads to an increased rate of damage development, as lateral expansion is interpreted to be the consequence of crack growth[57]. In addition, the rate of lateral expansion for damaged specimens was found to be greater at dynamic strain rates than at quasi-static strain rates, which indicates that crack growth is more sensitive to pre-existing damage in dynamic compression. Note also that four of the five damaged specimens tested in dynamic compression have strength values comparable to, if not higher than, the intact specimens tested in quasi-static compression, showing that the damaged specimens still exhibit rate-dependent strength. With increasing damage, the dynamic strength of the damaged specimens eventually fall below those of the quasi-static results for comparable damage levels. This suggests that, while there is a rate-dependent increase in the strength of damaged specimens, the rate-dependence decreases with increasing damage. The rate strengthening effect in ceramics is thought to be related to the increased nucleation of new cracks in intact material[58, 59, 38]. Therefore, with increasing damage, the energy required to nucleate new cracks likely supersedes the energy required to grow pre-existing cracks. In the damaged specimens, high-speed visualization of the dynamic failure process also showed that the solid regions, free of pre-existing cracks, sometimes exhibited

axial splitting. We believe this is caused by the nucleation of new cracks in the relatively undamaged regions, which eventually coalesce to form axial cracks. At the same time, the regions of the specimen with greater local crack damage are expected to fracture along preferentially oriented pre-existing cracks. This suggests that the rate effect may be related to the amount of crack-free volume within the damaged specimens.

In a similar study by Krimsky et al.[24], damaged boron carbide was found to be stronger under quasi-static compression than dynamic compression for similar levels of damage, as quantified by crack surface area. It is possible that the extent of pre-existing cracks for those specimens exceeded the threshold for which the rate effect is no longer active; thus, the strength is comparable at both rates. Furthermore, under quasi-static compression, the damaged specimens in that study experienced significant strength reductions in comparison to the intact specimens, indicating a high degree of damage. Note that the range of internal crack surface area probed in the present study and by Krimsky et al.[24] are comparable, however, given the differences in microstructure between the materials investigated in these studies (i.e., boron carbide in Krimsky et al.[24], and alumina in this study), the same level of crack damage is not expected to have the same effect on mechanical behavior.

4.3. Ballistic Performance of Damaged Ceramics

In this section, we discuss the mechanical response of damaged ceramics in the context of ballistic performance. We have shown in this study that the primary effects of crack damage in ceramics are to reduce the initial stiffness, initial rate of lateral expansion, and strength under compressive loading. A high stiffness is thought to contribute to ballistic performance by extending the duration of the dwell phase[60] and producing larger fragments which are believed to be more effective at eroding projectiles[61]. For a damaged ceramic, the low initial stiffness is expected to significantly degrade the dwell effect during a ballistic impact and may also lead to increased bending of the ceramic tile, which can cause undesirable fragmentation modes[62]. The reduced initial

rate of lateral expansion due to crack closure is also believed to be detrimental to ballistic performance as it effectively decreases the confining pressure from material expansion, and confinement has been shown to be an important factor for improving ballistic resistance[26, 63]. In the literature, the effects of compressive strength on ballistic performance have been more controversial. Some studies have correlated increased compressive strength to improved penetration resistance[64, 65] while others have assigned it a more minor role in determining ballistic performance[61, 66].

These observations motivate armor designs that incorporate greater confining pre-stress[67, 68, 69]. Increased axial and lateral confining pressure can serve to close up major cracks that form following an impact, allowing the ceramic to recover its intact stiffness and retain lateral confinement. In one study, Anderson et al.[11] conducted long rod penetration experiments on intact and pre-damaged silicon carbide targets confined in aluminum sleeves and found negligible differences in penetration velocities between intact and damaged targets. In addition, Horsfall and Buckley[70] conducted ballistic experiments on alumina tiles with large through-thickness cracks and found that the ballistic limit velocity was lowered by only 3%. In their experimental setup, the alumina tile was confined by a composite backing and a frontal spall shield. The small differences in performance between damaged and intact ceramics in these studies may be attributed to the confining pre-stress closing over cracks in the damaged specimens. Taken together, these results suggest that confinement is key to improving the durability and multi-hit capability of ceramic armors.

4.4. Computational Models for Ballistic Impacts

To simulate ballistic impacts on ceramics, it is necessary to account for the damaged state of ceramics. For instance, in the Rajendran-Grove micromechanics based impact model[71, 72, 73, 74], damage is tracked by increasing micro-crack density, and stiffness degrades as the material becomes progressively damaged. In the JH-1[55] and JH-2 models[56], both phenomenological models, damage is defined as accumulated plastic strain, and the material strength

degrades as the material transitions from intact to failed. The relationships between damage variables and degradation of mechanical properties are central to generating accurate predictions in impact models, as past investigators have emphasized[8, 75, 76, 77, 78]. However, little work has been done to experimentally connect physical measures of damage parameters to the degradation of mechanical properties[24]. In this study, we seek to fill this gap by providing quantitative characterization of the local and global strains related to the crack structures. Deformation mechanisms, including crack closure, expansion into existing cracks, and crack sliding, and their connections to the evolution of mechanical properties in damaged ceramics have been highlighted in this paper to elucidate the behavior of damaged ceramics and guide future model development. In addition, the qualitative observations of the differences in failure process for intact and damaged ceramics can also be used to validate model outputs. As an example, consider the damage models in the JH-1 model[55], which treats the transition from intact to failed as instantaneous, and the JH-2 model[56], which was later developed to account for a gradual transition from intact to failed. The strength results from this study suggest that the transition is gradual at dynamic strain rates.

5. Conclusion

Computational modeling of ballistic events is key to the development of advanced ceramic armor systems. This requires a clear understanding of the behavior of damaged ceramics. In this study, we investigated the effects of damage on the mechanical behavior of alumina, focusing on the connections between physical crack damage parameters and the degradation of mechanical properties. XCT was used to quantify internal crack networks, and DIC was used to characterize mechanical response. We visualized the local deformation mechanisms related to crack damage, including crack closure, opening, and sliding, and highlighted their connections to the evolution of global stress-strain behaviors in damaged ceramics. Lastly, high-speed photography was used to

visualize the difference in fracture behavior between intact and damaged alumina. Altogether, the results generated in this study expand our understanding of damaged ceramics and support future model development.

6. Acknowledgment

This research was sponsored by the Army Research Laboratory and was accomplished under Cooperative Agreement Number W91NF-16-2-0079 and W911NF-17-2-0213. The views and conclusions contained in this document are those of the authors and should not be interpreted as representing the official policies, either expressed or implied, of the Army Research Laboratory or the U.S. Government. The U.S. Government is authorized to reproduce and distribute reprints for Government purposes notwithstanding any copyright notation herein. The authors would also like to express their thanks to Bernie Faulkner, Rick Bubenko, Haoyang Li, and Kapil Bhagavathula for their help in conducting the experiments.

Research described in this paper was performed at the BMIT facility at the Canadian Light Source, which is supported by the Canada Foundation for Innovation, Natural Sciences and Engineering Research Council of Canada, the University of Saskatchewan, the Government of Saskatchewan, Western Economic Diversification Canada, the National Research Council Canada, and the Canadian Institutes of Health Research. We acknowledge Sergei Gasilov and Ning Zhu for their help in obtaining and reconstructing the XCT scans.

7. Data Availability

The raw/processed data required to reproduce these findings cannot be shared at this time as the data also forms part of an ongoing study.

References

[1] M. Mukasey, J. L. Sedgwick, D. Hagy, Ballistic resistance of body armor, nij standard-0101.06, US Department of Justice (www. ojp. usdoj. gov/nij).

[2] D. A. Shockey, A. Marchand, S. Skaggs, G. Cort, M. Burkett, R. Parker, Failure phenomenology of confined ceramic targets and impacting rods, International Journal of Impact Engineering 9 (3) (1990) 263–275.

[3] E. Strassburger, H. Senf, Experimental investigations of wave and fracture phenomena in impacted ceramics and glasses., Tech. rep., FRAUNHOFER-INST FUER KURZZEITDYNAMIK-ERNST-MACH-INST WEIL AM RHEIN (GERMANY) (1995).

[4] N. Bourne, J. Millett, Z. Rosenberg, On the origin of failure waves in glass, Journal of applied physics 81 (10) (1997) 6670–6674.

[5] N. Bourne, On the impact and penetration of soda-lime glass, International journal of impact engineering 32 (1-4) (2005) 65–79.

[6] Y. Partom, Modeling failure waves in glass, International journal of impact engineering 21 (9) (1998) 791–799.

[7] T. Behner, C. E. Anderson Jr, D. Orphal, V. Hohler, M. Moll, D. Templeton, Penetration and failure of lead and borosilicate glass against rod impact, International Journal of Impact Engineering 35 (6) (2008) 447–456.

[8] T. J. Holmquist, Some observations on the strength of failed ceramic, in: Advances in Ceramic Armor: A Collection of Papers Presented at the 29th International Conference on Advanced Ceramics and Composites, Jan 23-28, 2005, Cocoa Beach, FL, Vol. 296, John Wiley & Sons, 2009, p. 3.

[9] T. Holmquist, Analysis of the response of silicon carbide subjected to shock-reshock and shock-release plate-impact experiments, in: Journal de Physique IV (Proceedings), Vol. 134, EDP sciences, 2006, pp. 339–344.

[10] C. E. Anderson Jr, T. Behner, D. L. Orphal, A. E. Nicholls, D. W. Templeton, Time-resolved penetration into pre-damaged hot-pressed silicon carbide, International Journal of Impact Engineering 35 (8) (2008) 661–673.

[11] C. Anderson Jr, T. Behner, D. Orphal, A. Nickolls, T. Holmquist, Long-rod penetration into intact and pre-damaged sic ceramic, Tech. rep., SOUTHWEST RESEARCH INST SAN ANTONIO TX (2008).

[12] K. A. Dannemann, A. E. Nicholls, C. E. Anderson Jr, S. Chocron, J. D. Walker, Response and characterization of confined borosilicate glass: Intact and damaged, in: Advances in ceramic armor II, a collection of papers presented at the 30th int. conf. & exp. on advanced ceramics and composites, Vol. 27, 2006, p. 119e29.

[13] S. Chocron, C. E. Anderson Jr, K. A. Dannemann, A. E. Nicholls, N. L. King, Intact and predamaged boron carbide strength under moderate confinement pressures, Journal of the American Ceramic Society 95 (1) (2012) 350–357.

[14] C. E. Anderson Jr, Compression testing and response of sic-n ceramics: intact, damaged and powder, in: Advances in Ceramic Armor: A Collection of Papers Presented at the 29th International Conference on Advanced Ceramics and Composites, Jan 23-28, 2005, Cocoa Beach, FL, Vol. 296, John Wiley & Sons, 2009, p. 109.

[15] K. A. Dannemann, S. Chocron, A. E. Nicholls, C. E. Anderson Jr, Compressive damage development in confined borosilicate glass, Materials Science and Engineering: A 478 (1-2) (2008) 340–350.

[16] K. A. Dannemann, C. E. Anderson Jr, S. Chocron, J. F. Spencer, Damage development in confined borosilicate and soda-lime glasses, Journal of the American Ceramic Society 95 (2) (2012) 721–729.

[17] S. Chocron, C. E. Anderson Jr, A. E. Nicholls, K. A. Dannemann, Char-

acterization of confined intact and damaged borosilicate glass, Journal of the American Ceramic Society 93 (10) (2010) 3390–3398.

[18] S. Chocron, C. Anderson, K. Dannemann, A. Nicholls, Pressure effects on the compressive response of confined intact and damaged soda-lime glass, Experimental Mechanics 53 (1) (2013) 77–89.

[19] A. K. Zurek, D. A. Hunter, Dynamic testing and characterization of prefractured ceramic, in: AIP Conference Proceedings, Vol. 309, AIP, 1994, pp. 761–764.

[20] W. Chen, H. Luo, Dynamic compressive responses of intact and damaged ceramics from a single split hopkinson pressure bar experiment, Experimental mechanics 44 (3) (2004) 295–299.

[21] H. Luo, W. Chen, Dynamic compressive response of intact and damaged ad995 alumina, International Journal of Applied Ceramic Technology 1 (3) (2004) 254–260.

[22] H. Luo, W. W. Chen, A. Rajendran, Dynamic compressive response of damaged and interlocked sic–n ceramics, Journal of the American Ceramic Society 89 (1) (2006) 266–273.

[23] E. N. Landis, Toward a physical damage variable for concrete, Journal of engineering mechanics 132 (7) (2006) 771–774.

[24] E. Krimsky, K. Ramesh, M. Bratcher, M. Foster, J. D. Hogan, Quantification of damage and its effects on the compressive strength of an advanced ceramic, Engineering Fracture Mechanics 208 (2019) 107–118.

[25] C. Lo, T. Sano, J. D. Hogan, Microstructural and mechanical characterization of variability in porous advanced ceramics using x-ray computed tomography and digital image correlation, Materials Characterization (2019) 109929doi:https://doi.org/10.1016/j.matchar.2019.109929.
URL http://www.sciencedirect.com/science/article/pii/S104458031931441X

[26] C. E. Anderson Jr, S. A. Royal-Timmons, Ballistic performance of confined 99.5%-al203 ceramic tiles, International journal of impact engineering 19 (8) (1997) 703–713.

[27] J. Lankford, W. Predebon, J. Staehler, G. Subhash, B. Pletka, C. Anderson, The role of plasticity as a limiting factor in the compressive failure of high strength ceramics, Mechanics of Materials 29 (3-4) (1998) 205–218.

[28] N. Bourne, J. Millett, M. Chen, J. McCauley, D. Dandekar, On the hugoniot elastic limit in polycrystalline alumina, Journal of Applied Physics 102 (7) (2007) 073514.

[29] B. M. Koch, P. Jannotti, D. Mallick, B. Schuster, T. Sano, J. D. Hogan, Influence of microstructure on the impact failure of alumina, Materials Science and Engineering: A 770 (2020) 138549.

[30] A. Thompson, I. Maskery, R. K. Leach, X-ray computed tomography for additive manufacturing: a review, Measurement Science and Technology 27 (7) (2016) 072001.

[31] T. W. Wysokinski, D. Chapman, G. Adams, M. Renier, P. Suortti, W. Thomlinson, Beamlines of the biomedical imaging and therapy facility at the canadian light source-part 2, in: Journal of Physics: Conference Series, Vol. 425, IOP Publishing, 2013, p. 072013.

[32] Z. Wei, S. Wiebe, D. Chapman, Ring artifacts removal from synchrotron ct image slices, Journal of Instrumentation 8 (06) (2013) C06006.

[33] A. Khellaf, A. Beghdadi, H. Dupoisot, Entropic contrast enhancement, IEEE transactions on medical Imaging 10 (4) (1991) 589–592.

[34] K. V. Mardia, T. Hainsworth, A spatial thresholding method for image segmentation, IEEE transactions on pattern analysis and machine intelligence 10 (6) (1988) 919–927.

[35] J. Hsieh, et al., Computed tomography: principles, design, artifacts, and recent advances, SPIE Bellingham, WA, 2009.

[36] L. Vincent, Morphological area openings and closings for grey-scale images, in: Shape in Picture, Springer, 1994, pp. 197–208.

[37] T. S. Oesch, E. N. Landis, D. A. Kuchma, Conventional concrete and uhpc performance–damage relationships identified using computed tomography, Journal of Engineering Mechanics 142 (12) (2016) 04016101.

[38] B. Paliwal, K. Ramesh, An interacting micro-crack damage model for failure of brittle materials under compression, Journal of the Mechanics and Physics of Solids 56 (3) (2008) 896 – 923. doi:https://doi.org/10.1016/j.jmps.2007.06.012.
URL http://www.sciencedirect.com/science/article/pii/S0022509607001391

[39] M. L. Kachanov, A microcrack model of rock inelasticity part i: Frictional sliding on microcracks, Mechanics of Materials 1 (1) (1982) 19–27.

[40] H. Horii, S. Nemat-Nasser, Compression-induced microcrack growth in brittle solids: Axial splitting and shear failure, Journal of Geophysical Research: Solid Earth 90 (B4) (1985) 3105–3125.

[41] W. E. Lorensen, H. E. Cline, Marching cubes: A high resolution 3d surface construction algorithm, in: ACM siggraph computer graphics, Vol. 21, ACM, 1987, pp. 163–169.

[42] T. S. Newman, H. Yi, A survey of the marching cubes algorithm, Computers & Graphics 30 (5) (2006) 854–879.

[43] B. Pan, K. Qian, H. Xie, A. Asundi, Two-dimensional digital image correlation for in-plane displacement and strain measurement: a review, Measurement Science and Technology 20 (6) (2009) 062001.
URL http://stacks.iop.org/0957-0233/20/i=6/a=062001

[44] Y. Dong, B. Pan, A review of speckle pattern fabrication and assessment for digital image correlation, Experimental Mechanics 57 (8) (2017) 1161–1181. doi:10.1007/s11340-017-0283-1.
URL https://doi.org/10.1007/s11340-017-0283-1

[45] H. W. Schreier, J. R. Braasch, M. A. Sutton, Systematic errors in digital image correlation caused by intensity interpolation, Optical engineering 39.

[46] B. Pan, K. Qian, H. Xie, A. Asundi, Two-dimensional digital image correlation for in-plane displacement and strain measurement: a review, Measurement science and technology 20 (6) (2009) 062001.

[47] L. Mao, Z. Yuan, M. Yang, H. Liu, F.-p. Chiang, 3d strain evolution in concrete using in situ x-ray computed tomography testing and digital volumetric speckle photography, Measurement 133 (2019) 456–467.

[48] J. Lankford, Mechanisms responsible for strain-rate-dependent compressive strength in ceramic materials, Journal of the American Ceramic Society 64 (2) (1981) C-33–C-34. arXiv:https://ceramics.onlinelibrary.wiley.com/doi/pdf/10.1111/j.1151-2916.1981.tb09570.x, doi:10.1111/j.1151-2916.1981.tb09570.x.
URL https://ceramics.onlinelibrary.wiley.com/doi/abs/10.1111/j.1151-2916.1981.tb09570.x

[49] H. Horii, S. Nemat-Nasser, Overall moduli of solids with microcracks: load-induced anisotropy, Journal of the Mechanics and Physics of Solids 31 (2) (1983) 155–171.

[50] B. Paliwal, K. Ramesh, Effect of crack growth dynamics on the rate-sensitive behavior of hot-pressed boron carbide, Scripta materialia 57 (6) (2007) 481–484.

[51] J. D. Hogan, L. Farbaniec, M. Shaeffer, K. Ramesh, The effects of microstructure and confinement on the compressive fragmentation of an ad-

vanced ceramic, Journal of the American Ceramic Society 98 (3) (2015) 902–912.

[52] M. L. Batzle, G. Simmons, R. W. Siegfried, Microcrack closure in rocks under stress: direct observation, Journal of Geophysical Research: Solid Earth 85 (B12) (1980) 7072–7090.

[53] E. B. Eberhardt, Brittle rock fracture and progressive damage in uniaxial compression, Ph.D. thesis, University of Saskatchewan Saskatoon (1998).

[54] S.-H. Chang, C.-I. Lee, Estimation of cracking and damage mechanisms in rock under triaxial compression by moment tensor analysis of acoustic emission, International Journal of Rock Mechanics and Mining Sciences 41 (7) (2004) 1069–1086.

[55] G. Johnson, T. Holmquist, A computational constitutive model for brittle materials subjected to large strains, high strain rates and high pressures, Shock wave and high-strain-rate phenomena in materials (1992) 1075–1081.

[56] G. R. Johnson, T. J. Holmquist, An improved computational constitutive model for brittle materials, in: AIP conference proceedings, Vol. 309, AIP, 1994, pp. 981–984.

[57] H. Wang, K. Ramesh, Dynamic strength and fragmentation of hot-pressed silicon carbide under uniaxial compression, Acta Materialia 52 (2) (2004) 355–367.

[58] J. Lankford Jr., The role of dynamic material properties in the performance of ceramic armor, International Journal of Applied Ceramic Technology 1 (3) (2004) 205–210. arXiv:https://ceramics.onlinelibrary.wiley.com/doi/pdf/10.1111/j.1744-7402.2004.tb00171.x, doi:10.1111/j.1744-7402.2004.tb00171.x.
URL https://ceramics.onlinelibrary.wiley.com/doi/abs/10.1111/j.1744-7402.2004.tb00171.x

[59] K. Ravi-Chandar, W. G. Knauss, An experimental investigation into dynamic fracture: Iii. on steady-state crack propagation and crack branching, International Journal of Fracture 26 (2) (1984) 141–154. doi:10.1007/BF01157550.
URL https://doi.org/10.1007/BF01157550

[60] A. Krell, E. Strassburger, Hierarchy of Key Influences on the Ballistic Strength of Opaque and Transparent Armor, John Wiley and Sons, Ltd, 2009, pp. 45–55. arXiv:https://ceramics.onlinelibrary.wiley.com/doi/pdf/10.1002/9780470339695.ch4, doi:10.1002/9780470339695.ch4.
URL https://ceramics.onlinelibrary.wiley.com/doi/abs/10.1002/9780470339695.ch4

[61] A. Krell, E. Strassburger, Order of influences on the ballistic resistance of armor ceramics and single crystals, Materials Science and Engineering: A 597 (2014) 422–430.

[62] B. R. Lawn, D. B. Marshall, Nonlinear stress-strain curves for solids containing closed cracks with friction, Journal of the Mechanics and Physics of Solids 46 (1) (1998) 85–113.

[63] R. Woodward, W. Gooch Jr, R. O'donnell, W. Perciballi, B. Baxter, S. Pattie, A study of fragmentation in the ballistic impact of ceramics, International Journal of Impact Engineering 15 (5) (1994) 605–618.

[64] Z. Rozenberg, Y. Yeshurun, The relation between ballastic efficiency and compressive strength of ceramic tiles, International journal of impact engineering 7 (3) (1988) 357–362.

[65] Z. Rosenberg, Y. Ashuach, Y. Yeshurun, E. Dekel, On the main mechanisms for defeating ap projectiles, long rods and shaped charge jets, International journal of impact engineering 36 (4) (2009) 588–596.

[66] R. L. Woodward, A simple one-dimensional approach to modelling ceramic composite armour defeat, International Journal of Impact Engineering 9 (4) (1990) 455–474.

[67] D. Curran, L. Seaman, T. Cooper, D. Shockey, Micromechanical model for comminution and granular flow of brittle material under high strain rate application to penetration of ceramic targets, International Journal of Impact Engineering 13 (1) (1993) 53–83.

[68] O. Andersson, P. Lundberg, R. Renstrom, Influence of confinement on the transition velocity of silicon carbide, in: Proc. 23rd International Symposium on Ballistics, Tarragona, Spain, April, 2007, pp. 16–20.

[69] R. Chi, A. Serjouei, I. Sridhar, T. E. Geoffrey, Pre-stress effect on confined ceramic armor ballistic performance, International Journal of Impact Engineering 84 (2015) 159–170.

[70] I. Horsfall, D. Buckley, The effect of through-thickness cracks on the ballistic performance of ceramic armour systems, International journal of impact engineering 18 (3) (1996) 309–318.

[71] A. Rajendran, Modeling the impact behavior of ad85 ceramic under multiaxial loading, International Journal of Impact Engineering 15 (6) (1994) 749–768.

[72] A. Rajendran, D. Grove, Determination of rajendran-grove ceramic constitutive model constants, in: AIP Conference Proceedings, Vol. 370, AIP, 1996, pp. 539–542.

[73] A. Rajendran, D. Grove, Modeling the shock response of silicon carbide, boron carbide and titanium diboride, International Journal of Impact Engineering 18 (6) (1996) 611–631.

[74] D. Grove, A. Rajendran, Overview of the rajendran-grove ceramic failure model, Ceramic transactions 134 (2002) 371–382.

[75] C. E. Anderson Jr, A review of computational ceramic armor modeling, Proceedings of the 30.

[76] A. L. Tonge, K. Ramesh, Multi-scale defect interactions in high-rate brittle material failure. part i: Model formulation and application to alon, Journal of the Mechanics and Physics of Solids 86 (2016) 117–149.

[77] A. L. Tonge, K. Ramesh, Multi-scale defect interactions in high-rate failure of brittle materials, part ii: Application to design of protection materials, Journal of the Mechanics and Physics of Solids 86 (2016) 237–258.

[78] S. Dyachkov, A. Parshikov, M. Egorova, S. Y. Grigoryev, V. Zhakhovsky, S. Medin, Explicit failure model for boron carbide ceramics under shock loading, Journal of Applied Physics 124 (8) (2018) 085902.

List of Figures

1 (A) XCT scan of AD995 alumina. Due to the high resolution of the scan, small features are difficult to observe under low magnification. A magnified view of the center of the specimen is included on the right to show the internal crack. (B) 3D reconstruction of internal crack network showing the extent and inter-connectedness of the crack network. The red box outlines the boundary of the scan volume. 39

2 Stacked bar graph showing the crack surface area for each damaged specimen (D1 to D4). The quasi-static tests are denoted by QS and the dynamic tests are denoted by DYN. The divisions denote the area contribution of crack faces with different orientations to the loading axis. 40

3 Stress-strain and lateral-axial strain curves for intact and damaged specimens tested under (A) quasi-static and (B) dynamic compression. The quasi-static tests are denoted by QS and the dynamic tests are denoted by DYN. Intact tests are represented using dashed lines and denoted by IN while the damaged tests are represented using solid lines and denoted by D. The lateral-axial strain curves for QS D1, DYN D2, and DYN D4 are shown separately in insets so the evolution of the other curves is not dwarfed by the large lateral strains. 41

4 (A) Lateral contour plot of QS D1 showing the opening of a large axial crack. (B) Lateral contour plot of QS D3 showing a large axial crack that accommodates the expansion of adjacent solid material. (C) XCT scan of QS D4 cropped and filtered to show the crack network on the surface of the specimen. This image is overlaid with surface contours for QS D4 from (D) to (F) to show the location of localized strains in reference to the crack. (D) Axial contour plot of QS D4 showing localized compressive strains at lateral and low-angled inclined cracks. (E) Lateral contour plot of QS D4 showing the closing of axial and high-angled inclined cracks under compression. (F) Shear contour plot of QS D4 showing shear strains along inclined cracks. The white arrows are included to show relative motion of the crack surfaces. 42

5 (A) XCT scan of QS D4 showing the regions where axial and shear strains are queried. The regions of interest include (1 and 2) intact solid material, (3) an axial crack, (4 and 5) inclined cracks, (6) a triple junction, and (7) a lateral crack. (B) The evolution of axial strain at the regions of interest over time. (C) Shear strain development as a function of axial strain for each region of interest. 43

6 Stress-time histories of dynamic compression of intact (shown in black) and pre-damaged (shown in red) AD995 with high-speed video images showing failure process. Red arrows are used to indicate surface crack initiation points. 43

7 Transition strain plotted as a function of the crack surface area for orientations between 0° and 60° for each specimen. Blue points represent quasi-static results and red points represent dynamic results. 44

8 Compressive strength is plotted as a function of total crack surface area. Blue points represent quasi-static results and red points represent dynamic results. Diamonds indicate intact results and circles indicate damaged results. 44

8. Figures

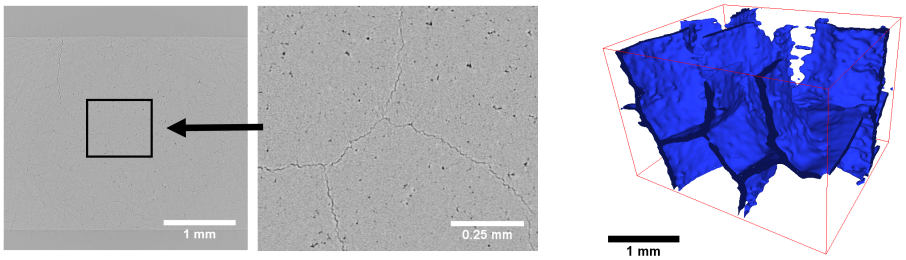

(A) (B)

Figure 1: (A) XCT scan of AD995 alumina. Due to the high resolution of the scan, small features are difficult to observe under low magnification. A magnified view of the center of the specimen is included on the right to show the internal crack. (B) 3D reconstruction of internal crack network showing the extent and inter-connectedness of the crack network. The red box outlines the boundary of the scan volume.

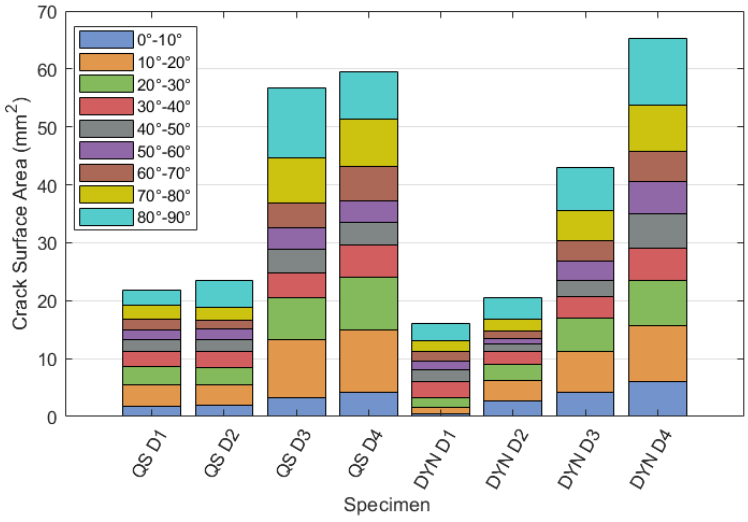

Figure 2: Stacked bar graph showing the crack surface area for each damaged specimen (D1 to D4). The quasi-static tests are denoted by QS and the dynamic tests are denoted by DYN. The divisions denote the area contribution of crack faces with different orientations to the loading axis.

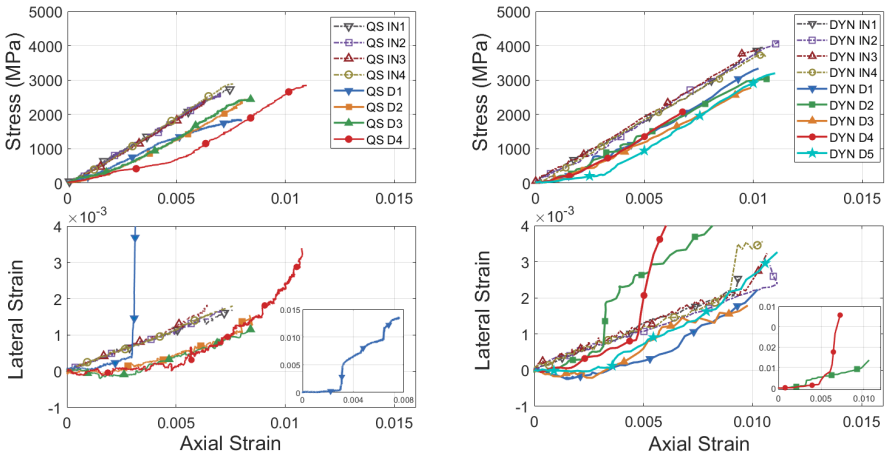

(A) (B)

Figure 3: Stress-strain and lateral-axial strain curves for intact and damaged specimens tested under (A) quasi-static and (B) dynamic compression. The quasi-static tests are denoted by QS and the dynamic tests are denoted by DYN. Intact tests are represented using dashed lines and denoted by IN while the damaged tests are represented using solid lines and denoted by D. The lateral-axial strain curves for QS D1, DYN D2, and DYN D4 are shown separately in insets so the evolution of the other curves is not dwarfed by the large lateral strains.

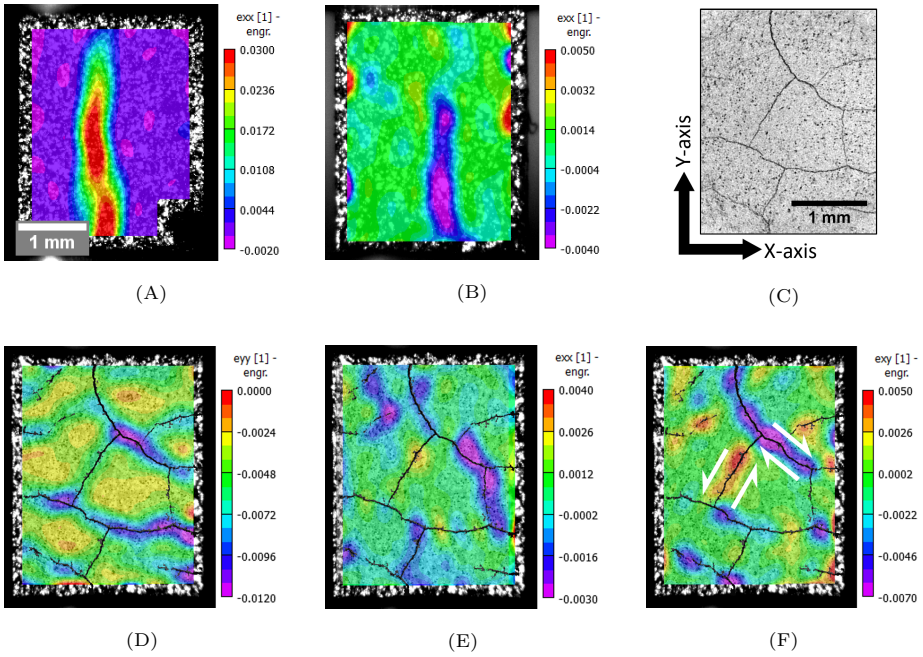

Figure 4: (A) Lateral contour plot of QS D1 showing the opening of a large axial crack. (B) Lateral contour plot of QS D3 showing a large axial crack that accommodates the expansion of adjacent solid material. (C) XCT scan of QS D4 cropped and filtered to show the crack network on the surface of the specimen. This image is overlaid with surface contours for QS D4 from (D) to (F) to show the location of localized strains in reference to the crack. (D) Axial contour plot of QS D4 showing localized compressive strains at lateral and low-angled inclined cracks. (E) Lateral contour plot of QS D4 showing the closing of axial and high-angled inclined cracks under compression. (F) Shear contour plot of QS D4 showing shear strains along inclined cracks. The white arrows are included to show relative motion of the crack surfaces.

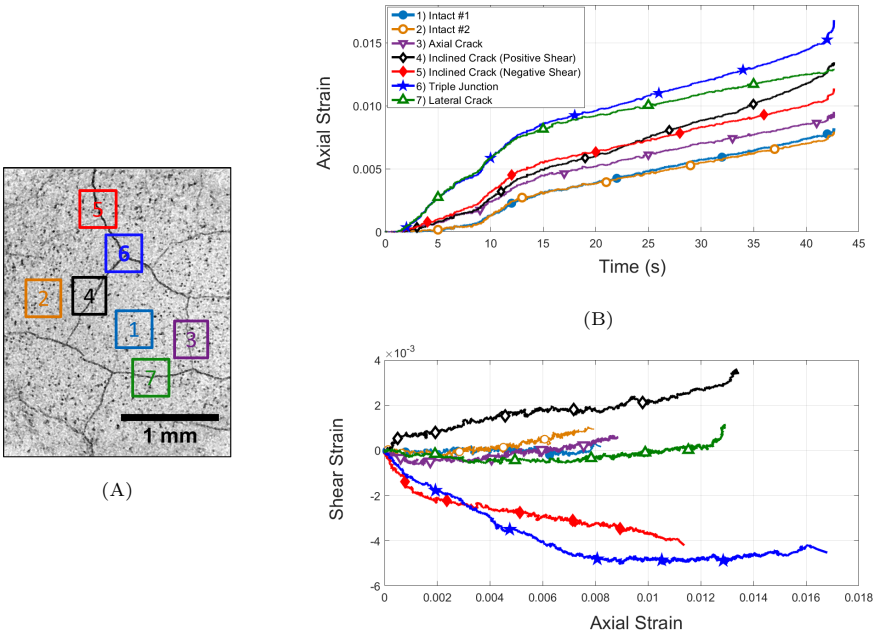

(A)

(B)

(C)

Figure 5: (A) XCT scan of QS D4 showing the regions where axial and shear strains are queried. The regions of interest include (1 and 2) intact solid material, (3) an axial crack, (4 and 5) inclined cracks, (6) a triple junction, and (7) a lateral crack. (B) The evolution of axial strain at the regions of interest over time. (C) Shear strain development as a function of axial strain for each region of interest.

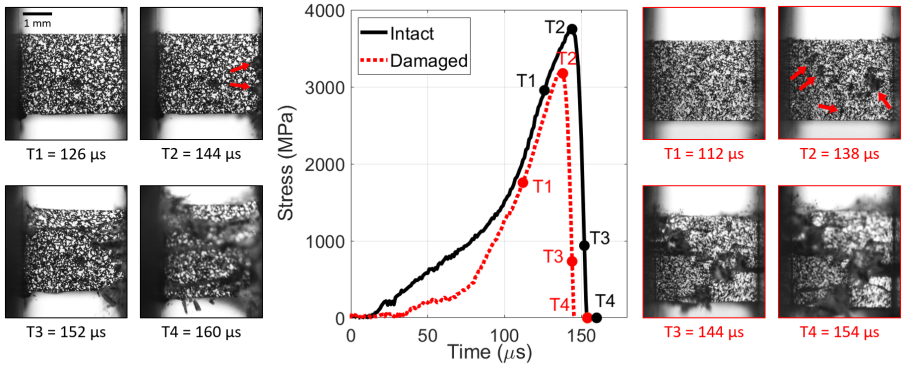

Figure 6: Stress-time histories of dynamic compression of intact (shown in black) and pre-damaged (shown in red) AD995 with high-speed video images showing failure process. Red arrows are used to indicate surface crack initiation points.

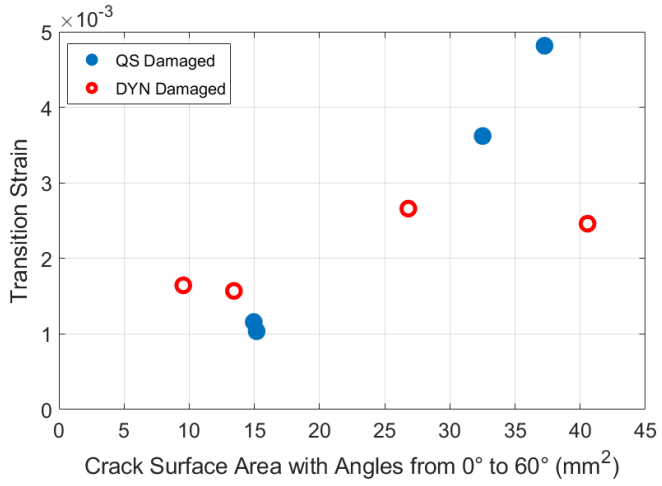

Figure 7: Transition strain plotted as a function of the crack surface area for orientations between 0° and 60° for each specimen. Blue points represent quasi-static results and red points represent dynamic results.

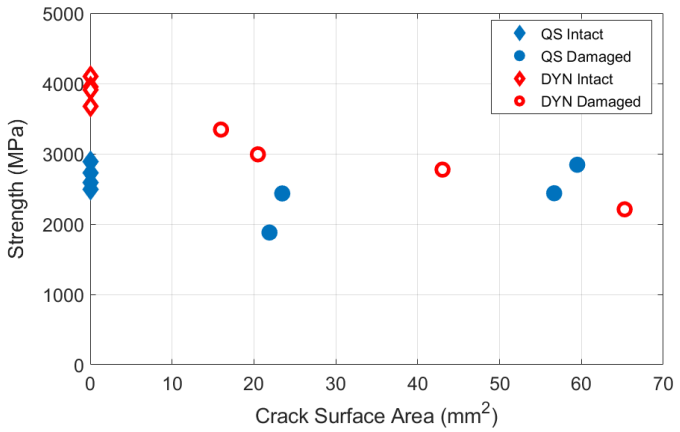

Figure 8: Compressive strength is plotted as a function of total crack surface area. Blue points represent quasi-static results and red points represent dynamic results. Diamonds indicate intact results and circles indicate damaged results.